

## Geophysical flows impacting a flexible barrier: effects of solid-fluid interaction

**Abstract** Flexible barriers undergo large deformation to extend the impact duration, and thereby reduce the impact load of geophysical flows. The performance of flexible barriers remains a crucial challenge because there currently lacks a comprehensive criterion for estimating impact load. In this study, a series of centrifuge tests were carried out to investigate different geophysical flow types impacting an instrumented flexible barrier. The geophysical flows modelled include covered in this study include flood, hyperconcentrated flow, debris flow, and dry debris avalanche. Results reveal that the relationship between the Froude number,  $Fr$ , and the pressure coefficient  $\alpha$  strongly depends on the formation of static deposits called dead zones which induce static loads and whether a run-up or pile-up impact mechanism develops. Test results demonstrate that flexible barriers can attenuate peak impact loads of flood, hyperconcentrated flow, and debris flow by up to 50% compared to rigid barriers. Furthermore, flexible barriers attenuate the impact load of dry debris avalanche by enabling the dry debris to reach an active failure state through large deformation. Examination of the state of static debris deposits behind the barriers indicates that hyperconcentrated and debris flows are strongly influenced by whether excessive pore water pressures regulate the depositional process of particles during the impact process. This results in significant particle rearrangement and similar state of static debris behind rigid barrier and the deformed full-retention flexible barrier, and thus the static loads on both barriers converge.

**Keywords** Geophysical flows · Solid-fluid interaction · Impact · Flexible barrier · Centrifuge modelling

### Introduction

Flexible barriers have been widely used to intercept various types of geophysical flows such as debris flows (Wendeler et al. 2006, 2007), open hillside avalanches (Kwan et al. 2014), rock avalanches (Sasiharan et al. 2006), and snow avalanches (Margreth and Roth 2008). Flexible barriers enable large deformation which prolongs the impact duration and reduces the impact load (Wendeler et al. 2006, 2007). Flexible barriers are advantageous because they occupy smaller footprints, are easier to construct on steep natural terrain, and are considered more sustainable structural countermeasures compared to reinforced concrete barriers. Relevant studies on the interaction of flexible barriers with geophysical flows focus on the structural response of a flexible barrier (Wendeler et al. 2006, 2007; Kwan et al. 2014), without examining the mesoscopic behaviour and dynamics of the geophysical flows. The dynamics of geophysical flows is fundamentally regulated by the interaction between the solid particles and thus the pore fluid pressure (Iverson 1997; Ng et al. 2016b; Song et al. 2017a). Intuitively, it is imperative to examine the impact process based on the dynamics of both the solid and fluid components to develop pertinent impact models.

A robust geophysical impact model is critical for conservative and cost-effective engineering protective structures. The impact model should be principally deduced from physical laws (e.g. conservation of mass, momentum, and energy) and verified using data collected using controlled physical experiments. Furthermore, the data should not be from the field given the natural idiosyncrasies involved in natural settings and natural materials (Iverson 2003, 2015). Challenges with well-controlled small-scale tests entail scaling disproportionalities in the rate of pore pressure dissipation in the flow and the degree of viscous and capillary stresses from the pore fluid (Iverson 2003). Furthermore, geomaterials are stress-state dependent (Schofield 1980; Ng 2014) and are difficult to replicate using small-scale settings.

In light of the limitations associated with field monitoring and scaling discrepancies in small-scale tests, the geotechnical centrifuge (Schofield 1980) provides an ideal means to study flow-barrier interaction. A series of centrifuge tests were carried out to investigate the effects of solid fraction of geophysical flows on the response of a rigid barrier by Song et al. (2017a). The solid fraction of the model flows was varied to cover a wide range of geophysical flows including flood, hyperconcentrated flow, debris flow, and dry debris avalanche. As a continuation of Song et al. (2017a), this study investigates various flow types impacting a model flexible barrier using the geotechnical centrifuge. A comparison is carried out between the test results of this study and rigid barrier tests carried out by Song et al. (2017a). Based on the comparison, the effects of solid-fluid interaction and barrier type on the impact response are elucidated.

### Estimation of impact force

#### Debris impact models

The estimation of debris impact force on structures is based on the conservation of momentum for hydrodynamic models and force equilibrium for hydrostatic models. Empirical coefficients are adopted within these models to account for discrepancies attributed to the simplifications and assumptions between theoretical predictions and physical measurements.

The most commonly adopted hydrodynamic approach for estimating the debris impact force,  $F$ , on barriers (Hungry et al. 1984; WSL 2009; Hübl et al. 2009; Kwan 2012) is given as follows:

$$F = \alpha \rho v^2 h w \quad (1)$$

whereas, the hydrostatic approach (Armanini 1997) is given as follows:

$$F = 0.5 \kappa \rho g h^2 w \quad (2)$$

where  $\alpha$  is pressure coefficient,  $\kappa$  is static pressure coefficient,  $\rho$  is the bulk density of flow ( $\text{kg/m}^3$ ),  $v$  is flow velocity (m/s), and  $h$  and  $w$  are the flow depth and width of the channel (m), respectively.

Aside from considering impact load of debris, boulders entrained within the flow mass and their induced loads are estimated separately. Boulder impact force is estimated using the Hertz equation which considers plastic deformation within the contact zone (Kwan 2012; Ng et al. 2016a) or flexural stiffness of structures (MLR 2006).

#### Relationship between Froude number and pressure coefficient

The aforementioned hydrodynamic and hydrostatic load models are indeed convenient for engineering purposes, but entail simplifications that are unable to capture key impact mechanisms observed in physical experiments such as run-up and pile-up (Choi et al. 2015), and dead zone formation (Gray et al. 2003). Based on the measured impact pressure of two-phase mixtures (sand and viscous liquid) along the height of the rigid barrier (Song et al. 2017a), results reveal a triangular pressure distribution instead of a uniform pressure distribution. A triangular pressure distribution is attributed to dead zones, observed using PIV in centrifuge tests, that contribute static load at the base of the barrier.

Ashwood and Hungr (2016) and Song et al. (2017a) reported that both static and dynamic loads should be considered during the impact process. Therefore, a more reasonable expression of the total impact load  $F$  induced on a barrier is given as follows:

$$F = 0.5\kappa' \rho g (\beta h)^2 w + \alpha' \rho v^2 h w \quad (3)$$

where  $\alpha'$  is the coefficient for dynamic effect only,  $\kappa'$  is the coefficient for static effect only, and  $\beta$  is the ratio between height of static debris and flow depth (see Fig. 3). Based on the conservation of momentum,  $\alpha'$  has a value of unity if only dynamic loading exists.

To further investigate the influence of the static load, the right hand side of Eqs. (1) and (3) are combined and rearranged as follows:

$$\alpha \rho v^2 h w = 0.5\kappa' \rho g (\beta h)^2 w + \alpha' \rho v^2 h w \quad (4)$$

$$\alpha = \frac{\kappa' \beta^2 g h}{2 v^2} + \alpha' \quad (5)$$

The term  $v^2/g h$  in Eq. (5) is the square of Froude number  $Fr^2$  which macroscopically quantifies the ratio between the inertial and gravitational forces:

$$Fr^2 = \frac{v^2}{g h} = \frac{\rho v^2}{\rho g h} \quad (6)$$

After substituting Eq. (6) into Eq. (5), Eq. (7) expresses the reciprocal of the relationship between pressure coefficient  $\alpha$  and  $Fr^2$

$$\alpha = \frac{\kappa' \beta^2}{2} \frac{1}{Fr^2} + \alpha' \quad (7)$$

From Eq. (7), it is apparent that  $\alpha$  becomes constant  $\alpha'$  when  $Fr^2$  tends towards infinity, indicating that the impact process is dominated by the dynamic component. As  $Fr^2$  approaches zero,  $\alpha$

tends towards infinity, therefore indicating  $\alpha$  is affected by the static component. Similarly, based on the relationship between  $Fr$  and  $\alpha$ , several studies based on physical tests and field monitoring data were amalgamated to deduced empirical relationships (Hübl et al. 2009; Cui et al. 2015). Hübl et al. (2009) elaborated that a hydrodynamic relationship (Eq. (1)) does not perform well at flows characterized using low  $Fr$  because the dynamic effect is less dominant compared to the static load.

#### Centrifuge modelling of geophysical flow impact

##### Scaling principle

Volumetric response of soils, more specifically dilatancy or contraction, is controlled by the effective stress. Changes in effective stress in turn regulate changes in pore water pressure (Iverson and George 2014). Centrifuge modelling ensures that the absolute stress states are correct between model and prototype by elevating the gravitational field  $N$  times. Scaling laws relevant to this study (Ng et al. 2016b) are summarized in Table 1.

Dimensionless group (Iverson 1997; Iverson 2015) ensures that relative ratios of stresses describing the solids and fluid of a geophysical flow are similar. The Savage number,  $N_S$ , characterizes the ratio of stress generated via instant grain collision and stress sustained under grain contact shear (Savage 1984; Iverson 1997):

$$N_S = \frac{p_s \dot{\gamma}^2 \delta^2}{(p_s - p_f)} \quad (8)$$

The Bagnold number,  $N_B$ , represents the ratio of stress generated via grain collision and viscous shear stress (Bagnold 1954):

$$N_B = \left[ \frac{v_s}{1 - v_s} \right] \frac{p_s \dot{\gamma} \delta^2}{\mu} \quad (9)$$

The inertial-diffusional time scale ratio characterizes the inertial time scale to pore fluid pressure diffusional time scale (Iverson 2015):

$$N_P = \frac{\sqrt{1/g}}{\mu h^2 / k E} \quad (10)$$

where  $\rho_s$  is the bulk density of solid grains ( $\text{kg/m}^3$ ),  $\rho_f$  is the bulk density of pore fluid ( $\text{kg/m}^3$ ),  $\dot{\gamma}$  is the shear rate ( $1/\text{s}$ ),  $\delta$  is the

**Table 1** Relevant scaling laws (22.4 g)

Parameter	Dimension	Scaling law (model/prototype)
Gravity	$L/T^2$	$N$
Density	$M/L^3$	1
Length	$L$	$1/N$
Velocity	$L/T$	1
Inertial time	$T$	$1/N$
Stress	$M/(T^2 L)$	1
Force	$ML/T^2$	$1/N^2$
Flexible barrier stiffness	$M/T^2$	$1/N$

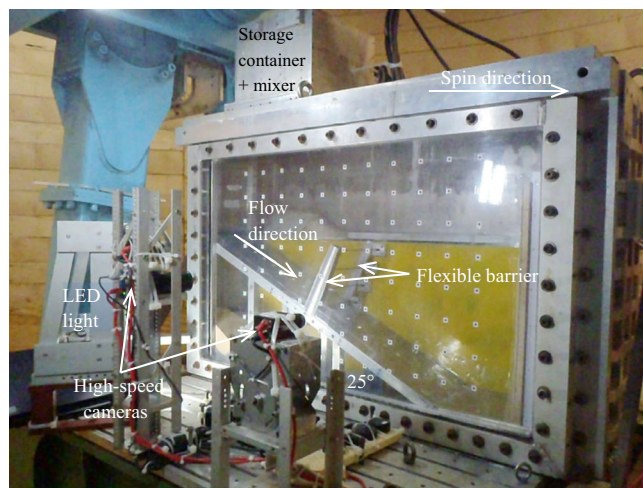
typical grain diameter (m),  $v_s$  is the volumetric solid fraction,  $\mu$  is the dynamic viscosity of pore fluid (Pas),  $l$  is the flow length (m),  $k$  is the intrinsic permeability ( $m^2$ ) as a function of  $v_s$ , and  $E$  is the bulk compressive stiffness of granular mixture (Pa). Details of the scaling of flow between model and prototype are described by Song et al. (2017a).

### Model setup

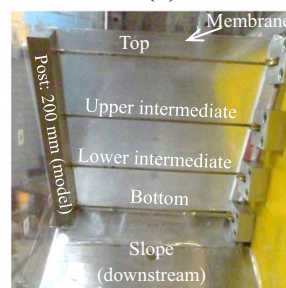
The centrifuge tests in this study were carried out at the Geotechnical Centrifuge Facility at the Hong Kong University of Science and Technology. The 400 g-ton centrifuge has an arm radius of 4.2 m (Ng 2014). The model container has plan dimensions of 1245 mm × 350 mm, and a depth of 851 mm. The Perspex of the model container and a partition wall are used to form a channelized slope within the model container (Fig. 1a). The slope has a channel width of 233 mm (5.2 m in prototype) and a length of 1000 mm (22.4 m in prototype), and is inclined at 25°. Mounted above the model slope is a storage container with a model volume of 0.03 m<sup>3</sup>. The storage container has a hinged door at the bottom that can be released in-flight using a hydraulic actuator. To prevent the consolidation of two-phase mixtures in-flight, a custom helical ribbon mixer is installed inside the storage container to provide continuous mixing.

A flexible barrier rigid post, 200 mm in height, is mounted 530 mm (11.9 m in prototype) from the most upstream end of the slope and sits flush against the Perspex (Fig. 1b). The rigid post has ball and socket connections to secure each model steel strand cable. In total, four cables span horizontally, namely top, upper intermediate, lower intermediate, and bottom cables, to form the face of the barrier. The other end of the horizontal cables pass through a partition via pulley systems and are attached to individual spring mechanisms. Each spring mechanism comprise one relaxed and one preloaded compression spring in series to model a bi-linear loading behaviour.

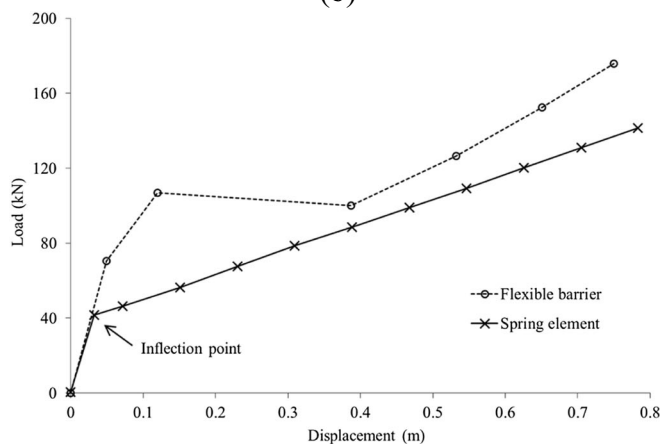
A simplified bi-linear loading behaviour of a horizontal cable is adopted (Fig. 1c). The load-displacement curve of a prototype flexible barrier cable with energy dissipating elements installed is compared with the loading response of a model barrier horizontal cable. The model barrier horizontal cable exhibits a distinct simplified bi-linear loading relationship. The slope  $K_1$  is steep, representing a stiff elastic response. The loading eventually reaches an inflection point, which is controlled by preloading the softer spring to a pre-specified value. The point of inflection is analogous to the activation of the energy dissipating elements in a prototype barrier. After the activation of energy dissipating elements, the loading curve exhibits a softer response ( $K_2$ ). Properties of the prototype flexible barrier are summarized in Table 2. The properties are further scaled down to model dimensions using scaling laws given in Table 1. A membrane is installed along the upstream face of the flexible barrier to act as a net that simulates the full retention of debris materials (fluid and particles) during impact. Although prototype barriers have some degree of permeability, the assumption adopted in this study simplifies the actual impact conditions to obtain fundamental insight for improving our understanding of flow-structure interaction. However, the assumption of full retention represents a conservative loading scenario for engineering designs (Ng et al. 2016c). Slack was provided in the high-stiffness membrane to ensure that the membrane would stretch out and not be subjected to tension under



(a)



(b)



(c)

**Fig. 1** a Side view of model setup on centrifuge platform; b model flexible barrier with rigid post, four horizontal cables, and membrane; c load-displacement behaviour of flexible barrier cable (Ng et al. 2016b, c, in prototype)

impact. This helps ensure that the load is fully transmitted to the horizontal cables. The effective width of flexible barrier is 203 mm (4.5 m in prototype). Details of the model flexible barrier system are described by Ng et al. (2016b).

### Instrumentation

Load cells were installed along each horizontal cable to measure the induced axial forces. Laser sensors with a resolution of 0.2 mm were used in conjunction with the spring mechanisms of the

**Table 2** Properties of flexible barrier (all dimensions in prototype)

Flexible barrier	Stiffness (kN/m)	Inflection point (kN)
Top cable	$K_1 = 2.6 \times 10^3$ $K_2(k_c) = 2.0 \times 10^2$	40
Upper, lower intermediate, and bottom cables	$K_1 = 1.8 \times 10^3$ $K_2(k_c) = 2.0 \times 10^2$	40

flexible barrier model to measure cable displacement synchronously with the force measurement. A high-speed camera with a resolution of  $1300 \times 1600$  pixels at a sampling rate 640 fps was used (Fig. 1a). The influence of solid fraction on velocity attenuation and deposition processes behind the barrier was analysed using Particle Image Velocimetry (PIV) analysis (White et al. 2003; Take 2015). Illumination to capture high-speed images was achieved by using two 1000 W LED lights.

### Two-phase materials

The prototype flows in this study were simplified as ideal two-phase flows. These flows comprise pure viscous pore fluid and uniform sand. The fluid phase represents the water-fine grain mixture which flows freely between the grains (solid phase). As aforementioned, dimensionless numbers in the centrifuge model should match those in prototype. By reducing the grain diameter ( $\delta$ ) and the pore fluid viscosity ( $\mu$ )  $N$  times, similarity is achieved using the dimensionless group (Song et al. 2017a).

Leighton Buzzard (LB) fraction C sand is used for the granular assembly and characterized fairly uniform with diameters of about 0.6 mm (Choi et al. 2015). LB fraction C sand has internal friction angle is  $31^\circ$ . A prototype dynamic viscosity of 0.5 Pas (Zhou and Ng 2010) was adopted in this study. This corresponds to a viscosity of 0.022 Pas in model scale. The density of the viscous liquid closely resembles water ( $1000 \text{ kg/m}^3$ ). The bulk density of the dry sand held within the storage area is about  $1530 \text{ kg/m}^3$  and sand-liquid mixture densities are summarized in Table 5.

### Test programme and procedure

To investigate the influence of solid-fluid interaction on the impact behaviour of geophysical flows, the solid fraction is varied as 0.0, 0.2, 0.4, 0.5, and 0.58 (Table 3). The solid fraction of the liquid saturated flows is limited to 0.5 in this study because of the limitation of the mixing system under an elevated gravitational condition in the centrifuge. Note that in test FS with a solid fraction 0.58, the interstitial fluid is air, but nevertheless can still be classified as a saturated flow. The volume of flows in this study is equivalent to  $170 \text{ m}^3$  in prototype.

**Table 3** Test programme and testing materials (all dimensions in model scale)

Test ID	Solid fraction $v_s$	Material
FL	0.00	Viscous liquid (0.022 Pas)
FSL20	0.20	LB fraction C sand (0.6 mm)
FSL40	0.40	+ viscous liquid (0.022 Pas)
FSL50	0.50	
FS	0.58	LB fraction C sand (0.6 mm) + air (0.000018 Pas)

Once the model was prepared, the centrifuge was spun up to  $22.4 \times g$ . The interaction time was scaled down to  $1/22.4$  of prototype conditions. To account for this, a high sampling rate of 20 kHz was selected to capture the kinematic and dynamic processes. After readings stabilized, the storage container door released by the hydraulic actuator. The geophysical flows transitioned on to the slope and impacted the barrier. The cable force, cable elongation, and high-speed imagery were recorded synchronously. After the debris mass reached a static state, the centrifuge was spun down.

### Characterization of flow regime

Prior to conducting impact tests, a series of calibration tests without a barrier were carried out at  $22.4 \times g$ . The flows in this study were characterized using the Savage number,  $N_S$ , Bagnold number,  $N_B$ , inertial-diffusional time scale ratio,  $N_D$  and the square of Froude number,  $Fr^2$ , at the location along the channel where the barrier would be installed. According to Savage and Hutter (1989), the flows in this study are in a grain contact dominated regime ( $N_S < 0.1$ ) rather than a collisional regime. For test FS, grain collision dominates over viscous effect according to the threshold reported by Bagnold (1954), specifically  $N_B < 40$  to 450. However, the collisional stresses had a rather minor influence as indicated by the  $N_S$  (Song et al. 2017a). The characterization of the flow regimes is summarized in Table 4. The inertial-diffusional time scale ratio is discussed later.

The influence of solid fraction on the Froude characterization is shown in Fig. 2. The development of velocity, flow depth, and Froude regime depends on the potential height between the position of storage container and the barrier. In this study, with the fixed potential height, subcritical Froude condition ( $Fr < 1$ ) was not achieved. Test results show a sudden change in  $Fr^2$  when solid grains (0.2 solid fraction) are introduced to the flow from pure liquid flow. The abrupt change in  $Fr^2$  reflects a significant influence of the solid fraction on debris mobility. As the solid fraction is increased from 0.2 (test FSL20), the  $Fr^2$  progressively decreases, indicating a lower sensitivity to changes in solid fraction (Song et al. 2017a). Laboratory and field evidence shows a transition from flood to hyperconcentrated flow occurs when the solid fraction achieves a minimum value of 0.03 to 0.1 (Pierson 2005). Moreover, typical solid fractions for saturated debris flows are higher than 0.4 (Iverson and George 2014). To attain a comprehensive understanding of the entire spectrum of geophysical flows impact on structures, this study (see Fig. 2) covers the range from flood (test FL), hyperconcentrated flow (test FSL20), debris flow (test FSL40 and FSL50), and dry debris avalanche (test FS). The major difference of these flow types lies in the varying degree of solid-fluid interaction in regulating the flow and impact behaviour.

### Experimental results

#### Impact mechanism

PIV analysis was carried out (Fig. 3a, b) from the high-speed images of test FSL50 when the peak force was measured. The flow direction is from left to right. The flood (FL), hyperconcentrated flow (FSL20), and debris flow (FSL40 and FSL50) can be characterized as a run-up mechanism (Choi et al. 2015). The vertical jet travels along the barrier without an obvious attenuation in velocity. The debris eventually overflows the barrier and reaches static



**Table 4** Flow regime of the modelled flows

Test ID	Solid fraction ( $v_s$ )	Froude number ( $Fr/Fr^2$ )	Savage number ( $N_s$ )	Bagnold number ( $N_B$ )	Inertial-diffusional time scale ratio ( $N_p$ )	Inertial-settling time scale ratio ( $N_{Settle}$ )
FL	0.00	13.9/193	NA	0	0	NA
FSL20	0.20	6.6/44	$1.5 \times 10^{-2}$	5	$6.5 \times 10^1$	1.3
FSL40	0.40	5.0/25	$9.9 \times 10^{-3}$	11	$5.6 \times 10^{-1}$	3.0
FSL50	0.50	3.6/13	$4.5 \times 10^{-3}$	11	$3.4 \times 10^{-2}$	4.7
FS <sup>a</sup>	0.58	4.4/19	$4.9 \times 10^{-3}$	$2.4 \times 10^4$	$5.5 \times 10^0$	$6.9 \times 10^4$

<sup>a</sup> Note the pore fluid of test FS is air and the viscosity of air is adopted accordingly

state as a free surface levels out. The solid particles final deposition surface of run-up mechanism is nearly horizontal and the deposition height depends on the solid fraction, with debris flow (FSL50) impact the maximum. By contrast, the dry debris avalanche (FS) can be characterized as a pile-up mechanism. The dry granular debris layers on top of the previous deposited material. The high degree of grain contact shearing and shear resistance of the dry sand flow rapidly attenuate flow energy and the deposition height only reaches half of the barrier height (Ng et al. 2016; Song et al. 2017a; Wendeler 2016; Wendeler and Volkwein 2015).

Although the flood (FL), hyperconcentrated flow (FSL20), and debris flow (FSL40 and FSL50) can be characterized as run-up mechanisms, whereby an enlarging dead zone forms with the increasing solid fraction (see PIV analysis result of FSL50 in Fig. 3b). For hyperconcentrated flow (FSL20), there is no obvious dead zone forming at the barrier base during the impact process coherent deposits are not apparent until the flow reaches a static state. The differences in the deposition processes are attributed to the role of solid fraction in the transition from viscous-dominated to friction-dominated regimes (Bagnold 1954; Takahashi 2014).

**Cable elongation and barrier deflection**

The large deformation of a flexible barrier is the key feature for attenuating impulse loads from the debris and entrained boulders. Impact on the flexible barrier induces substantial barrier deflection (bulging in Fig. 3a). In order to deduce the barrier deflection

and impact load acting on the flexible barrier, a mathematical representation of the deformed horizontal cable is necessary. Since the debris impact pressure is always perpendicular to the barrier face, a circular curve provides the best approximation of a deformed cable under debris impact pressure (Fig. 4, Sasiharan et al. 2006). The pressure,  $p$ , acting on a circular curve can be decomposed into uniform  $p$  across the initial cable length  $L$  and uniform  $p$  along the deflection  $D$ . Note that most literature

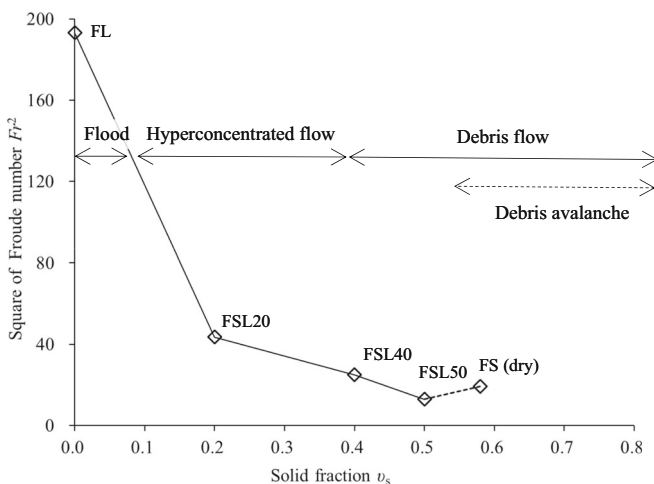


**Fig. 2** Influence of solid fraction  $v_s$  on square of Froude number  $Fr^2$ . Geophysical flow types are distinguished by solid fraction  $v_s$

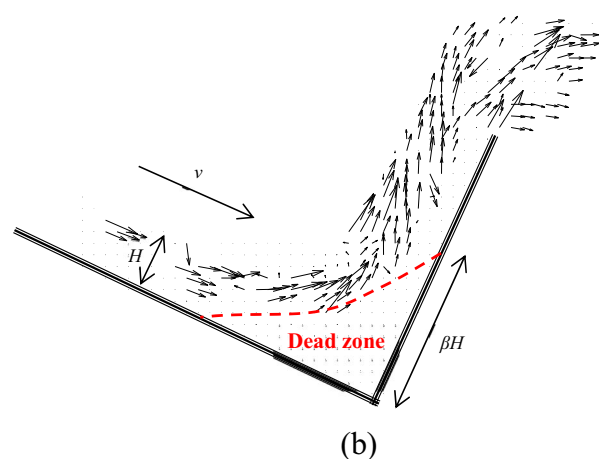
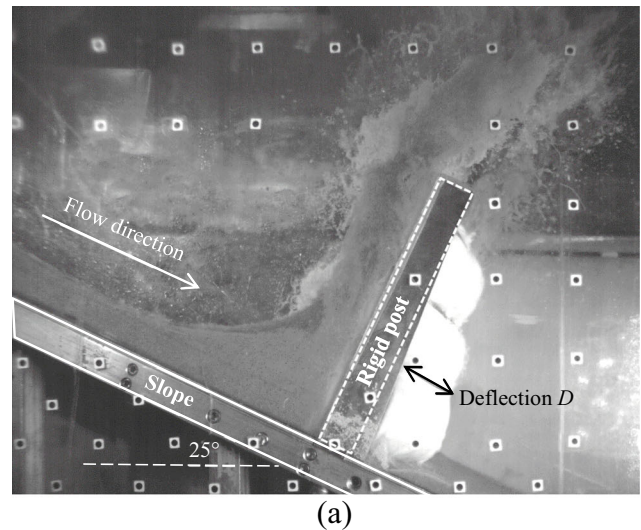


**Fig. 3** a Captured run-up mechanism of FSL50 at maximum normal force; b PIV analysis result showing a dead zone behind the barrier (deflection is not shown)

assumes a horizontally distributed  $p$  on the initial length  $L$  (approximated as a parabola curve or a catenary curve (Ng et al. 2016c)) and the vertical component is neglected. This assumption is acceptable for impact with negligible barrier deflection. However, as the deflection increases, a circular representation is more appropriate.

The cable elongation of a flexible barrier is crucial for investigating barrier loading behaviour and is rarely recorded by the large-scale tests (DeNatale et al. 1999; Bugnion and Wendeler 2010) and field monitoring (Wendeler et al. 2006, 2007; Kwan et al. 2014). The cable elongation of this experimental study is measured synchronously with cable force. Typical cable elongation for test FSL50 is shown for the top, upper intermediate, lower intermediate, and bottom cables in Fig. 5a. All dimensions are in prototype scale unless stated otherwise. The initial impact time of all the tests are readjusted to 1.0 s in prototype. The maximum elongation, 1.3 m, occurs in the lower intermediate cable but is similar to that of the bottom cable. The elongation of the top and upper intermediate cables decreases with the barrier height.

The deflection,  $D$ , is defined as the maximum value occurring at the middle of the deformed cable (Fig. 4). The deflection trend (Fig. 5b) is similar with that of the cable elongation. Yet the magnitude of the deflection is even larger, reaching 1.5 m (33% of cable length  $L$ ) for the lower intermediate cable. After reaching the peak deflection, the measurement of deflection only exhibits a minor rebound. This is because the static load is maintained behind the flexible barrier after the dynamic impact.

#### Cable force and normal impact force

The bottom and lower intermediate cables pick up loading upon initial impact of test FSL50 (Fig. 6a). While the top and upper intermediate cables do not record loading until the run-up reaches the upper part of barrier. The cable loads between 1.0 and 2.5 s of the impact process show a high degree of fluctuation as the second stage of the bi-linear loading curve is being triggered (Fig. 1c).

As shown in Fig. 4, the decomposition of the cable force  $T$  includes a component normal to the barrier face  $T_1$  and a

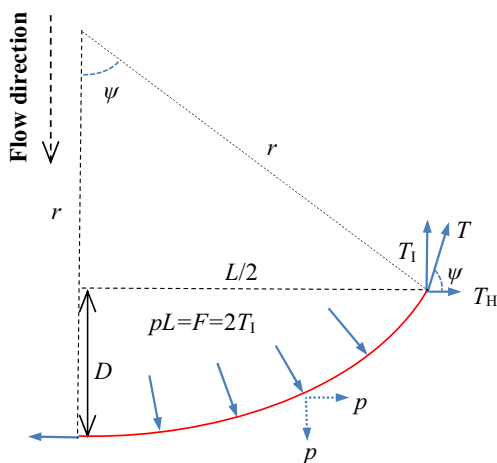


**Fig. 4** Diagram of a deflected horizontal cable under distributed load  $pL = F$  along the chord of a circular curve. Because of symmetry, only half of the cable is shown

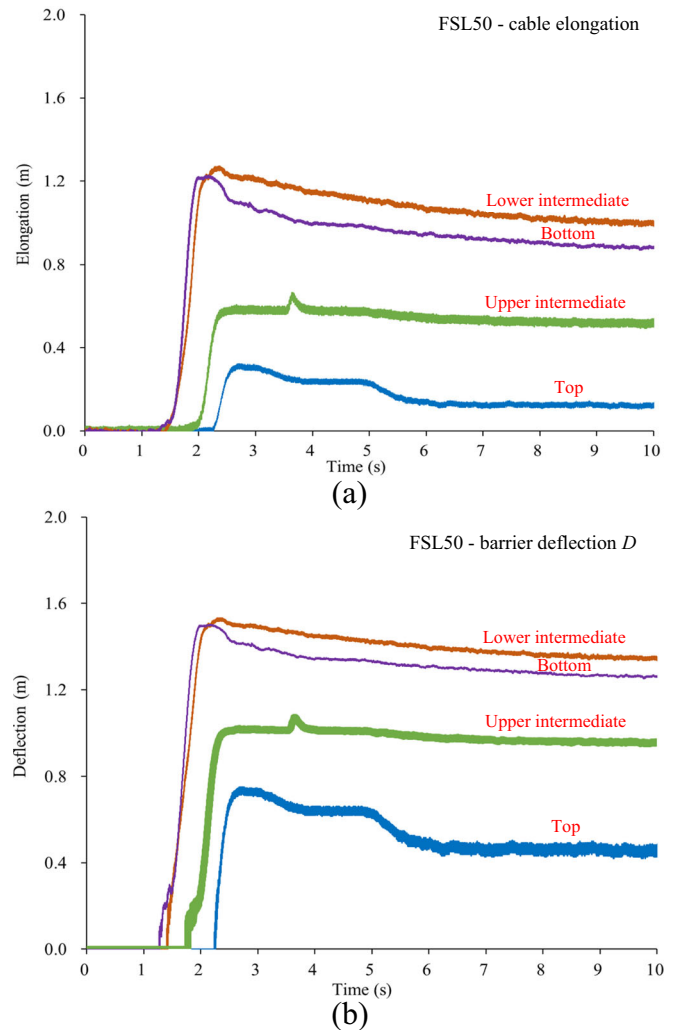


**Fig. 5** a Cable elongation time history of FSL50; b barrier deflection  $D$  time history. (all dimensions in prototype)

horizontal component  $T_H$  Song et al. 2017, Debris flow impact on flexible barrier: effects of debris-barrier stiffness and flow aspect ratio (Submitted to Landslides). The normal components  $T_1$  on the right and left sides of a flexible barrier cable give the impact load induced by the flow. While the horizontal components  $T_H$  on both sides counterbalance each other since they are the same in magnitude but in opposite directions. The  $T_1$  time histories for all four horizontal cables are shown in Fig. 6b. The summation of  $T_1$  for each cable is the total impact load  $F$ . Details of the normal impact loads on a rigid barrier (Song et al. 2017a) are also shown for comparison in Figs. 6b and 8, and Table 5 to highlight the barrier type effect.

The horizontal component  $T_H (= T \cos \psi)$  of the cable force  $T$  is shown in Fig. 6c, where  $\psi$  is the angle of deflection (Fig. 4). The summation of the four horizontal components is also shown. Comparing with the normal impact force  $T_1 (= T \sin \psi$ ; Fig. 6b), the horizontal component  $T_H$  is much lower in magnitude. However, this is not always the case and the magnitude depends on the stiffness and deflection of the barrier. With increasing stiffness, the deflection angle  $\psi$  will tend towards zero. As a consequence, the horizontal component  $T_H$  will exceed the normal component  $T_1$ .

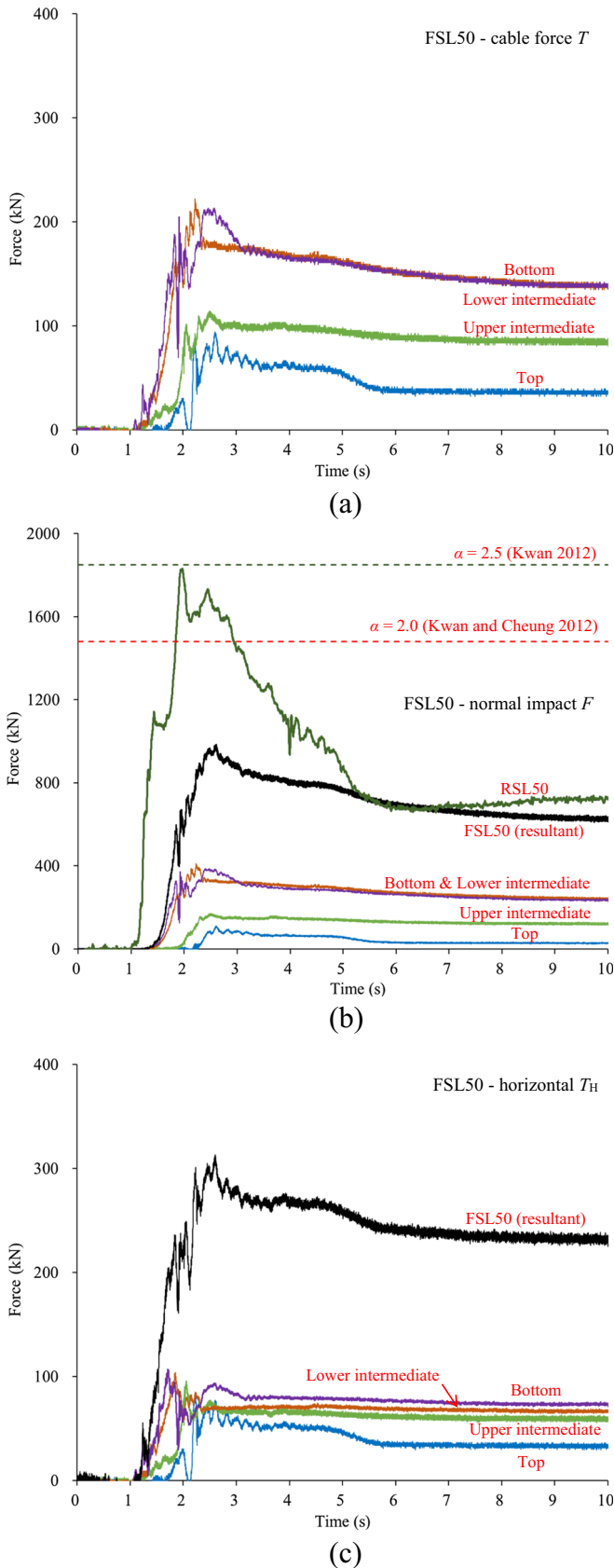


**Fig. 6** a Measured cable force  $T$  time history for test FSL50; b normal component  $F = 2T$ , of the cable force  $T$ ; comparison between the resultant normal force and the total force on rigid barrier (RSL50); c horizontal component  $T_H$  of the cable force  $T$ . (all dimensions in prototype)

This implies that a lower barrier stiffness favours low cable force and the integrity of the flexible barrier system.

The normal loading behaviour of each flexible barrier cable, i.e. relationship between the cable deflection  $D$  and the normal impact load  $F$ , is shown in Fig. 7. The normal load of the cable  $F$  is normalized by  $k_c L$ , where  $k_c$  is the cable stiffness (the second stage in Fig. 1c), and the deflection  $D$  is normalized by half of cable length  $L/2$ . The normal impact force  $F$  increases with deflection  $D$  with an increasing rate. The theoretical line is the predicted loading behaviour with a single linear cable stiffness (the second stage in Fig. 1c). Although a bi-linear stiffness was adopted, the measured loading behaviour of the four cables follows the theoretical line. This indicates that as the cable force far exceeds the inflection point of the bi-linear loading behaviour, the contribution of the first stage stiffness on the overall barrier response tends negligible. However, for those small-volume events, the cable force may not reach inflection point (not mobilize the energy dissipating element in prototype barrier). The relationship discussed in Fig. 7 is not applicable.

### Effects of barrier type

#### Normal load profiles at peak force

The time histories of the normal load on each flexible barrier cable and the summation of the cable loads as the total impact load for tests FSL20, FSL40, and FS are compared (Fig. 8). The total forces of the rigid barrier tests conducted by Song et al. (2017a) are also shown for comparison. The normal loads of each cable at the occurrence of peak force (Fig. 8) are plotted against the cable position in Fig. 9. The normal impact forces are normalized by the predicted total force via the hydrodynamic approach (Eq. (1)) with  $\alpha = 1.0$ ; meanwhile, the position of each cable is nondimensionalized by the flow depth  $h$  of each test. The triangular normal load distribution is generally similar with the pressure distribution of that corresponding to the rigid barrier tests. However, the key difference is that the impact loads for the two bottom cables are close to each other. Unlike the rigid barrier where the whole structure bears the impact pressure, the pressure on the flexible barrier membrane would further transfer to the horizontal cables. The bottom cable only bears the load transferred from the membrane on one side of the cable. While the load on the lower intermediate cable is a superposition of distributed impact load from both sides of the cable. As a result, the impact load acting on the lower intermediate cable is close to that on the bottom cable.

The lower half (bottom two cables) of barrier bears the majority of total peak load. For tests FL, FSL20, FSL40, FSL50, and FS, the proportions of peak load by the lower half to the total load are 64, 81, 73, 73, and 91%, respectively. For a triangular load distribution on rigid barrier, 75% of the load is taken by the lower half of the barrier. The percentages of the load taken by the lower half of rigid and flexible barriers are relatively close. Yet more load is redistributed to the lower intermediate cable for a flexible barrier (Fig. 9) since it bears loads from both sides of the cable.

#### Pressure coefficient

The peak load induced on the rigid barrier tests is more obvious than those of the flexible barrier (Figs. 6b and 8). Compared

**Table 5** Peak force and dynamic pressure coefficient

Test ID	Flexible	Rigid (Song et al. 2017a)	Interaction mechanism	Bulk density (kg/m <sup>3</sup> )	Frontal velocity (m/s)	Peak force (kN)		Peak force ratio $F_{flex}/F_{rigid}$	Dynamic pressure coefficient	
						$F_{flex}$	$F_{rigid}$		$\alpha_{flex}$	$\alpha_{rigid}$
FL		RL	Run-up compressible	1000	36.2	811	1735	0.5	0.2	0.3
FSL20		RSL20	Run-up	1330	18.4	1228	1662	0.7	0.7	0.8
FSL40		RSL40	Run-up	1660	13.3	913	1938	0.5	0.9	1.6
FSL50		RSL50	Run-up	1825	10.1	983	1830	0.5	1.3	2.2
FS		RS	Pile-up active mode	1530	11.8	286	659	0.4	0.2	0.7

with the rigid barrier tests of flood (RL), hyperconcentrated flow (RSL20), and debris flow (RSL40 and RSL50), the peak loads on flexible barrier are attenuated by up to 50% due to the effect of low stiffness for flexible barrier. The reduction in the peak loads is due to the large deflection and extended interaction duration of flexible barrier. The peak loads of both series of tests are summarized in Table 5.

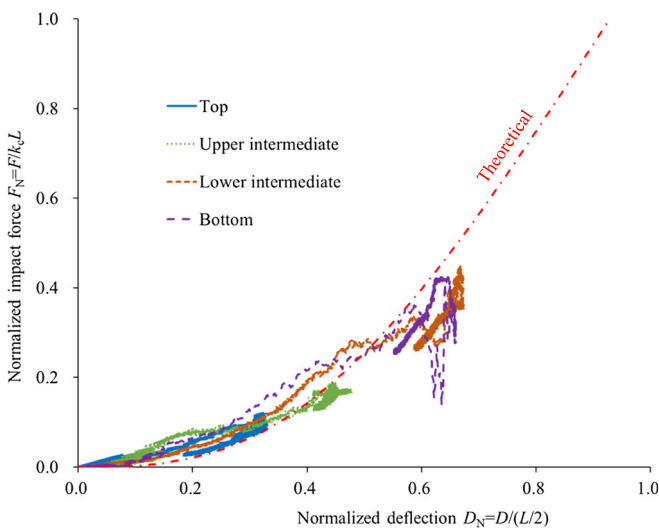
The relationship between square of Froude number  $Fr^2$  and pressure coefficient  $\alpha$  is summarized (Fig. 10). The pressure coefficient  $\alpha$  (Eq. (1)) is deduced based on the peak impact force of each test. The data points for the flood (FL), hyperconcentrated flow (FSL20), and debris flow (FSL40 and FSL50) follow the theoretical  $Fr^2$ - $\alpha$  relationship described in Eq. (7), i.e. high  $\alpha$  value corresponds to the gravitationally induced static load at low  $Fr^2$  regime. However, for the dry debris impact (FS and RS), the  $Fr^2$  is close to that of debris flow (FSL50 and RSL50), but the deduced  $\alpha$  values are much lower and do not follow the  $Fr^2$ - $\alpha$  relationship. This difference stems from the fact that for a pile-up impact mechanism, the dry debris barely

runs up along the barrier and the peak load generated is close to the static load.

At high Froude numbers,  $\alpha$  values are less influenced by gravity and are closer to unity. However,  $\alpha$  values for floods (FL, 0.2; and RL, 0.3) are much lower than the theoretical prediction (conservation of momentum) at high  $Fr^2$ . This is because at high  $Fr^2$  and low solid fraction, the modelled flows entrain air along the flow path. The air is compressed during the impact process and extends the interaction duration (Peregrine 2003), and thus subsequently reduces the impact load.

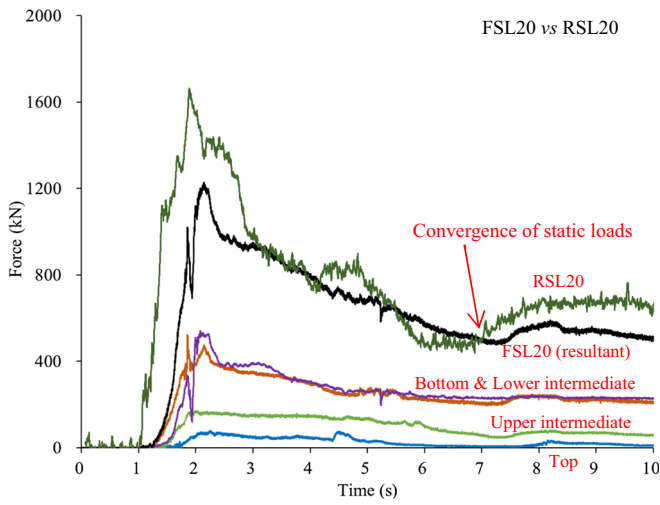
As mentioned previously, this study aims to cover the flow types ranging from flood, hyperconcentrated flow, debris flow, to the dry granular avalanche. From the observed impact kinematics (Song et al. 2017a and this study), a smooth transition from run-up to pile-up mechanism is expected with an enlarging dead zone at the barrier base. This indicates that a distinct relationship between the  $Fr^2$  and  $\alpha$  does not exist (Fig. 10). This is quite evident for the dry debris (FS and RS) tests which conflict with the tests with 50% solid fraction (FSL50 and RSL50). Dry debris avalanche is also a two-phase flow; however, the viscous contribution from air is significantly less than that of the viscous liquid. Surely, a more comprehensive relationship is required to properly characterize the solid-fluid interaction. Two reference lines are shown for tests RSL50 ( $\alpha = 2.5$  for rigid barrier design, Kwan 2012) and FSL50 ( $\alpha = 2.0$  for flexible barrier design, Kwan and Cheung 2012). Note that the recommended values are constant, rather than dependent on the  $Fr^2$ . Both of the deduced values from this study (2.2 and 1.3, Table 5) are lower than the design recommendations.

Figure 10 also compares the peak loads of each rigid-flexible impact pair. The abscissa is nondimensionalized as the Froude number, while the peak force is normalized by  $\rho v^2 h w$  (Eq. (1)) as  $\alpha$  in the ordinate. Results show that, regardless of the impact mechanism,  $\alpha$  values of flexible barrier tests are generally lower than the rigid barrier counterparts. This is because of the difference in stiffness of rigid and flexible barriers. Furthermore, from test FL to FSL50, the difference between  $\alpha$  values for each pair of tests increases. This indicates that flexible barrier is more efficient at stopping flows with high solid fraction. The flows with high solid fraction have high grain contact stresses and are more efficient at dissipating the kinetic energy through grain contact shearing. The flexible barrier further enhances the energy dissipation through its

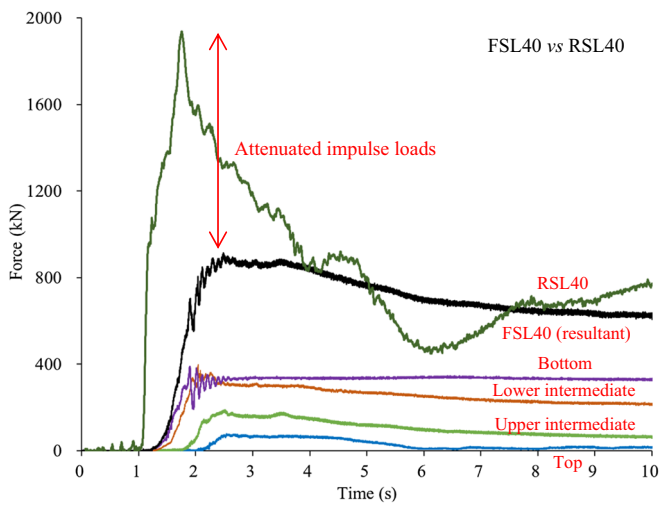


**Fig. 7** Normal loading behaviour of the horizontal cables ( $D$ - $F$  relationship). The normal load  $F$  is normalized by  $k_c L$ , where  $k_c$  is the cable stiffness, and deflection  $D$  is normalized by half of cable length  $L/2$ . Drop in the bottom cable corresponds to the fluctuation in Fig. 6a

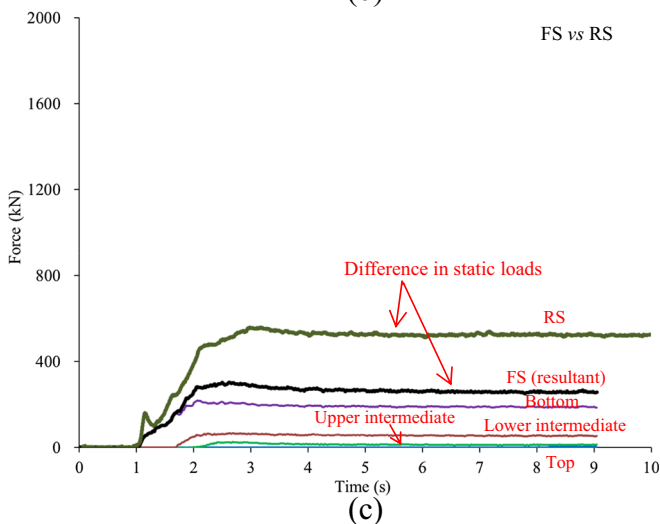




(a)



(b)



(c)

**Fig. 8** Comparison of normal force time history for flexible and rigid barrier tests: **a** FSL20 vs RSL20; **b** FSL40 vs RSL40; **c** FS vs RS. FSL50 vs RSL50 is shown in Fig. 6b

large deformation and hence more effective internal shearing (mixing) within the flows.

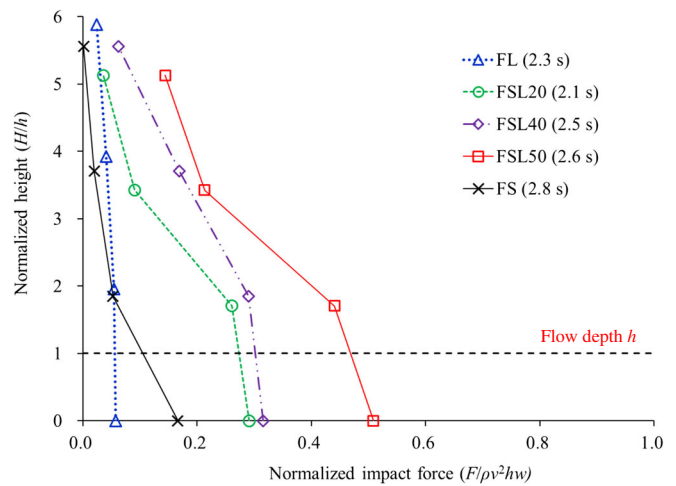


**Fig. 9** Normal load profiles at the occurrence of peak normal force  $F$ . The variation in normalized height  $H/h$  is caused by the variation in flow height  $h$

### Effects of solid-fluid interaction

#### Comparison of static loads

As expected, the peak loads acting on the rigid and flexible barriers differ. However, the static loads of the flood, hyperconcentrated flow, and debris flow behind both barriers converge with each other (Figs. 6b and 8a, b). Moreover, the peak loads of the dry debris avalanche (FS and RS), resulting from a pile-up mechanism, are the same as the static loads (“hardening” behaviour), but the static load on flexible barrier no longer converges with that on rigid barrier (Fig. 8c). The flexible barrier deflects substantially during the impact process and the movement of the boundary induces shear stress inside the granular material. An examination of the static state of the debris is carried out in this section.

The solid phase is regulated by the fluid phase, the hyperconcentrated flow (FSL20), and debris flow (FSL40 and

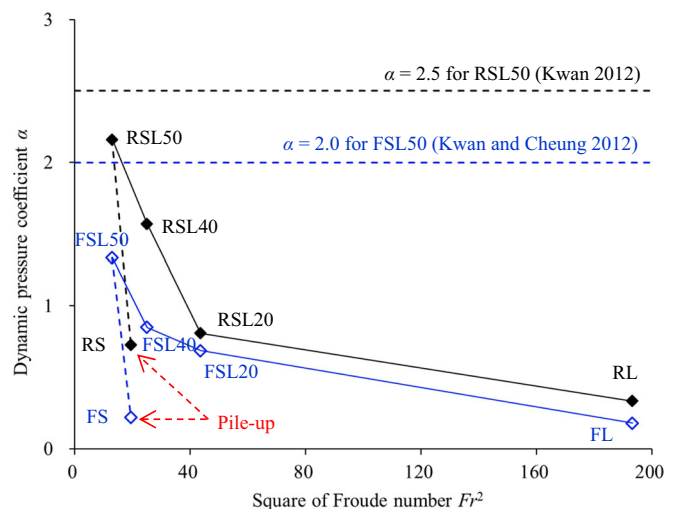


**Fig. 10** Relationship between  $Fr^2$  and  $\alpha$  based on the hydrodynamic approach. Because of the pile-up impact mechanism, the  $\alpha$  values of tests FS and RS do not follow the general trend of  $Fr^2$ - $\alpha$  relationship

FSL50) deposition angle between the horizontal plane and the free surface of the static deposit is close to zero, whereas, the dry debris (FS) deposition angle is close to its internal friction angle. Aside from the deposition angle, the deposition heights of all tests differ from each other. This indicates that it is not proper to examine the state of debris by directly comparing their absolute values of static loads. Instead, the measured static load behind the barriers is compared with its reference active load based on Coulomb earth pressure theory (Fig. 11).

Data points lying around each dashed line fitted from origin denote that they are at a similar state. The diagonal line denotes the theoretical Coulomb active failure ( $k_a$ ) state of the static debris. In this way, the static state of tests with different absolute values can be compared. Even though considerable lateral movement of flexible barrier occurs, the state of hyperconcentrated flow (FSL20) and debris flow (FSL40 and FSL50) behind the flexible barrier is similar to that of the rigid barrier (Fig. 11) and is still far away from the active failure state ( $k_a$ ). This explains the convergence of static loads of hyperconcentrated flow (FSL20) and debris flow (FSL40 and FSL50) behind the rigid and flexible barriers.

With the increase of solid fraction, for the rigid barrier tests (including test RS), there is an obvious trend that the state of the debris behind the rigid barrier approaches towards active state ( $k_a$ ). Despite this trend, the static debris of test RS is still far away from the active state. By contrast, test FS reaches the active failure state ( $k_a$ ) because of the large deflection of flexible barrier (effect of low barrier stiffness). The barrier is displaced subject to the progressive pile-up process. The displacement in turn leads to the development of an active lateral earth pressure, thereby minimizing the load acting on the barrier (Ng et al. 2016b). The positive feedback mechanism between the displacement of the barrier and the reduction in lateral earth pressure permits the dry debris to remain in the active failure state.

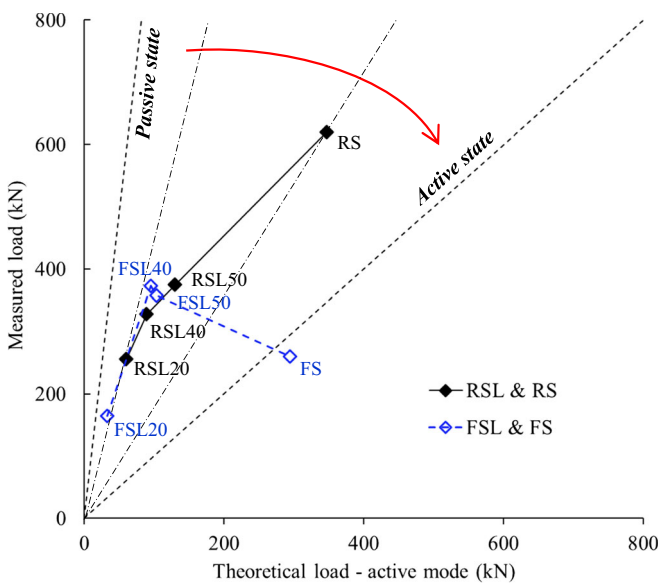


**Fig. 11** Relationship between the measured static loads and the loads at active failure mode for both flexible and rigid barrier tests. The state of debris at static condition tend to the active mode with the increase of solid fraction and grain contact stress

**Particle rearrangement and stress history**

Two processes are involved during the impact process: (1) debris downslope motion; (2) pore fluid pressure dissipation as solid particles settle down. The pore fluid pressure dissipation and solid particle settlement are two aspects of the solid-fluid segregation, but with difference emphases. Pore fluid pressure dissipation emphasizes the pore fluid draining through the soil skeleton, while particle settlement refers to the relative movement of particles in the pore fluid under the influence of gravity. The process of pore fluid pressure dissipation has been described by Iverson and George (2014) and Iverson (2015), etc. to quantify whether the pore fluid pressure is sustained before reaching the deposition area. The  $N_p$  (Eq. (10)) is developed to quantify the ratio between the time scales of debris downslope motion and pore pressure dissipation. In principle, as the solid fraction increases, the intrinsic permeability  $k$  (in  $m^2$ ) reduces accordingly. As a result, the time scale for the pore fluid pressure dissipation will be extended. In Table 4, however,  $N_p$  does not demonstrate an expected decreasing trend. This is because  $N_p$  only characterizes the influence of the solid phase on the pore fluid drainage (relative movement to the solid phase), but cannot reflect the particle settlement and rearrangement (relative movement to the fluid phase) under the influence of viscous fluid.

The fluid phase has a relatively greater influence on the geophysical flow behaviour compared to the solid phase when the solid fraction is relatively low and particles are suspended within the fluid, e.g. FSL20 vs FSL40 in this study. Hence,  $N_p$  can be enhanced to reflect the particle movement in the fluid phase, specifically the settlement of solid phase. The maximum settlement height (Fig. 12):

$$h_{settle} = \frac{v_{s,max} - v_s}{v_{s,max}} h \tag{11}$$

where  $v_{s,max}$  is the maximum solid fraction and is assumed to be 0.6 (Iverson and George 2016) in this study. According to the Stokes' law, the fine particles settle slower and will reach steady state velocity (Iverson 1997) shortly after settlement commences:

$$v_{settle} = \frac{(\rho_s - \rho_f)g\delta^2}{18\mu} \tag{12}$$

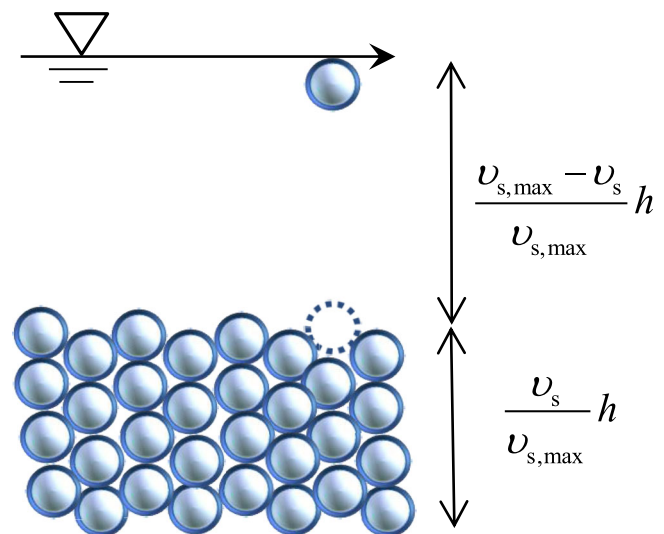


**Fig. 12** Illustration of the maximum settling height  $h_{settle}$ . Low solid fraction mixtures have larger maximum  $h_{settle}$

The time scale of a single particle to reach the final deposition surface (Fig. 12) is adopted to quantify the settlement time scale:

$$t_{\text{Settle}} = \frac{18(v_{s,\text{max}} - v_s)\mu h}{(\rho_s - \rho_f)v_{s,\text{max}}g\delta^2} \quad (13)$$

The inertial-settling time scale ratio quantifies the ratio of time scales of the flow downslope motion (impact) and the fine particle settlement within the fluid:

$$N_{\text{Settle}} = \frac{\sqrt{l/g}}{18(v_{s,\text{max}} - v_s)\mu h / (\rho_s - \rho_f)v_{s,\text{max}}g\delta^2} \quad (14)$$

From Eq. (14), the time scale for particle rearrangement (process of settlement) reduces substantially as the solid fraction increases. The estimated  $N_{\text{Settle}}$  values for tests FSL20, FSL40, FSL50, and FS are also summarized in Table 5. For the dry debris avalanche impact, due to the close packing of the solid particles, particle rearrangement at the barrier base is completed before the actual impact process. As grain contact stresses dominate the flow, the induced shear stresses caused by downstream movement remain within the final deposition. In other words, the stress history of flowing debris influences the final static load behind the rigid barrier. As a result of the internal shear stress, the state of static debris is closer to the active failure state (see RS in Fig. 11). With the further contribution of large flexible barrier deflection, the state of test FS fully reaches active failure state (Fig. 11).

The deposition process of particles in hyperconcentrated flow (FSL20) and debris flow (FSL40 and FSL50) is completed after the impact process, so that the particles deposit behind a deformed barrier. The stress history of the flowing debris has less influence on the final static load behind the flexible barrier. As a result of the long settlement time scale and the rearrangement of the solid phase in both hyperconcentrated flow (FSL20) and debris flow (FSL40 and FSL50), the state of debris behind the deflected flexible barrier has no significant difference with that observed behind a rigid barrier (Fig. 11). Note that to distinctly investigate the stiffness effect, the model flexible barrier is idealized as a full-retention (or low-permeability) barrier. With the permeability of flexible barrier considered, the results in Fig. 11 may tend to shift to the active state line. Further investigation should be carried out to quantify the effects of barrier permeability.

Understanding the deposition process behind a barrier can shed light on and facilitate a more cost-effective design, i.e. the active state of the debris on a flexible barrier denotes the minimum lateral load. However, due to the unpredictable properties of geophysical flows, especially the solid fraction, adopting an active state for the static debris behind a deformed flexible barrier may pose as a non-conservative design. Given the unpredictable solid fraction of geophysical flows and the complex state of the static debris, it is recommended that the design of the static load on both rigid and flexible barriers should be based on the  $k_o$  condition.

## Conclusions

A series of centrifuge tests studying geophysical flows impacting a flexible barrier were carried out. The flow types cover flood, hyperconcentrated flow, debris flow, and dry debris avalanche. The dynamic response of a flexible barrier was compared with that of a rigid barrier. Key findings from this study are drawn as follows:

- (a) For debris flow (50% solid fraction) impacting a flexible barrier, 73% of the peak impact load is taken by the two cables at the bottom of barrier. Similarly, for a rigid barrier with a triangular load distribution, the lower half of rigid barrier carries 75% of the peak impact load. Furthermore, tests reveal an approximate triangular impact load distribution along the height of barrier, but with the values of bottom two cables close to each other. This indicates that flexible barriers redistribute loading to the upper cables of the barrier.
- (b) Theoretically, pressure coefficient  $\alpha$  tends towards infinity as square of Froude number  $Fr^2$  approaches zero. However, experimental results show that the relationship between  $Fr^2$  and  $\alpha$  depends on both the static load behind the barrier and whether a predominately run-up or pile-up mechanism develops. Pressure coefficient  $\alpha$  values drop from test with 50% solid fraction (FSL50, debris flow) to dry debris avalanche impact (FS). This is because of the distinct pile-up impact mechanism where the dry debris barely runs up along the barrier and the peak load is close to the static load.
- (c) The effect of low flexible barrier stiffness is quantified and compared with rigid barrier test results. Due to a prolonged impact duration for the flexible barrier, the peak loads for flexible barriers are reduced by up to 50% for flood, hyperconcentrated flow, and debris flows, when compared with a rigid barrier. By contrast, the load attenuation mechanism for the dry debris avalanche is different. The substantial deformation of flexible barrier enables the dry debris behind the flexible barrier to reach an active failure ( $k_a$ ) state. The active failure state is a result of both the barrier deformation and the high frictional contact grain stresses of dry debris avalanche.
- (d) The static loads of hyperconcentrated flow and debris flow on a full-retention flexible barrier converge with those on a rigid barrier. This is because the state of static debris is similar with that of the debris behind rigid barrier, despite the large barrier deformation. For hyperconcentrated flow and debris flow, solid particles are largely rearranged during settlement process due to high degree of solid-fluid interaction. A revised dimensionless number, inertial-settling time scale ratio, is proposed to quantify the degree of particle rearrangement and maintenance of the shear stress history. Given the unpredictable solid fraction of geophysical flows and the complex state of the static debris, the design of the static load on both rigid and flexible barriers should be conducted based on  $k_o$  condition.

## Acknowledgements

The authors are grateful for financial support from research grant T22-603/15-N provided by the Research Grants Council of the Government of Hong Kong SAR, China and the HKUST Jockey Club Institute for Advanced Study for their support. The authors acknowledge the support from the Chinese Academy of Sciences (CAS) Pioneer Hundred Talents Program (Song Dongri) and the Youth Innovation Promotion Association, CAS. Also financial supports from the National Natural Science Foundation of China (grant no. 11672318) and the International partnership program of Chinese Academy of Sciences (grant no. 131551KYSB20160002) are greatly appreciated.

## References

- Armanini A (1997) On the dynamic impact of debris flows. In *Recent developments on debris flows* (pp. 208–226). Springer, Berlin Heidelberg
- Ashwood W, Hungr O (2016) Estimating the total resisting force in a flexible barrier impacted by a granular avalanche using physical and numerical modeling. *Can Geotech J*. doi:10.1139/cgj-2015-0481
- Bagnold RA (1954) Experiments on a gravity-free dispersion of large solid spheres in a Newtonian fluid under shear. *Proc R Soc London A Math Phys Eng Sci* 225(1160):49–63
- Bugnion L, Wendeler C (2010) Shallow landslide full-scale experiments in combination with testing of a flexible barrier. In *Monitoring, simulation, prevention and remediation of dense and debris flows III*, pp 161–173
- Choi CE, Au-Yeung SCH, Ng CWW, Song D (2015) Flume investigation of landslide granular debris and water runoff mechanisms. *Geotech Lett* 5:28–32
- Cui P, Zeng C, Lei Y (2015) Experimental analysis on the impact force of viscous debris flow. *Earth Surf Process Landf*. doi:10.1002/esp.3744
- DeNatale JS, Iverson RM, Major JJ, LaHusen RG, Fiegel GL, Duffy JD (1999) Experimental testing of flexible barriers for containment of debris flows. US Department of the Interior, US Geological Survey
- Gray JMNT, Tai YO, Noelle S (2003) Shock waves, dead zones and particle-free regions in rapid granular free-surface flows. *J Fluid Mech* 491:161–181
- Hübl J, Suda J, Proske D, Kaitna R, Scheidl C (2009) Debris flow impact estimation. In *Proceedings of the 11th International Symposium on Water Management and Hydraulic Engineering*, pp. 1–5. Ohrid, Macedonia
- Hung O, Morgan GC, Kellerhals R (1984) Quantitative analysis of debris torrent hazards for design of remedial measures. *Can Geotech J* 21(4):663–677
- Iverson RM (1997) The physics of debris flows. *Rev Geophys* 35(3):245–296
- Iverson RM (2003) How should mathematical models of geomorphic processes be judged? In: Wilcock PR, Iverson RM (eds) *Prediction in geomorphology*. American Geophysical Union, Washington
- Iverson RM (2015) Scaling and design of landslide and debris-flow experiments. *Geomorphology* 244:9–20
- Iverson RM, George DL (2014) A depth-averaged debris-flow model that includes the effects of evolving dilatancy. I. Physical basis. *Proc R Soc London A Math Phys Eng Sci* 470(2170):20130819
- Iverson RM, George DL (2016) Modelling landslide liquefaction, mobility bifurcation and the dynamics of the 2014 Oso disaster. *Geotechnique* 66:175–187
- Kwan JSH (2012) Supplementary technical guidance on design of rigid debris-resisting barriers. GEO Report No. 270. Geotechnical Engineering Office, HKSAR Government
- Kwan JSH, Cheung RWM (2012) Suggestion on design approaches for flexible debris-resisting barriers. Discussion note DN1/2012. Geotechnical Engineering Office, HKSAR Government
- Kwan JSH, Chan SL, Cheuk JCY, Koo RCH (2014) A case study on an open hillside landslide impacting on a flexible rockfall barrier at Jordan Valley, Hong Kong. *Landslides* 11(6):1037
- Margreth S, Roth A (2008) Interaction of flexible rockfall barriers with avalanches and snow pressure. *Cold Reg Sci Technol* 51(2):168–177
- MLR (2006) Specification of geological investigation for debris flow stabilization. DZ/T 0220-2006, National Land Resources Department, China, 32 p (in Chinese)
- Ng CWW (2014) The state-of-the-art centrifuge modelling of geotechnical problems at HKUST. *J Zhejiang Univ Sci A* 15(1):1–21
- Ng CWW, Choi CE, Su Y, Kwan JSH, Lam C (2016a) Large-scale successive boulder impacts on a rigid barrier shielded by gabions. *Can Geotech J* 53(10):1688–1699
- Ng CWW, Song D, Choi CE, Koo RCH, Kwan JSH (2016b) A novel flexible barrier for landslide impact in centrifuge. *Geotech Lett*:221–225
- Ng CWW, Song D, Choi CE, Liu LHD, Kwan JSH, Koo RCH, Pun W (2016c) Impact mechanisms of granular and viscous flows on rigid and flexible barriers. *Can Geotech J* 54(2):188–206
- Pierson TC (2005) Hyperconcentrated flow-transitional process between water flow and debris flow. In *Debris-flow hazards and related phenomena* (pp. 159–202). Springer, Berlin Heidelberg
- Peregrine DH (2003) Water-wave impact on walls. *Annu Rev Fluid Mech* 35(1):23–43
- Savage SB, Hutter K (1989) The motion of a finite mass of granular material down a rough incline. *J Liq Mech* 199:177–215
- Schofield AN (1980) Cambridge geotechnical centrifuge operations. *Geotechnique* 30(3):227–268
- Sasiharan N, Muhunthan B, Badger TC, Shu S, Carradine DM (2006) Numerical analysis of the performance of wire mesh and cable net rockfall protection systems. *Eng Geol* 88(1):121–132
- Savage SB (1984) The mechanics of rapid granular flows. *Adv Appl Mech* 24:289–366
- Song D, Ng CWW, Choi CE, GGD Z, Kwan JSH, Koo RCH (2017a) Influence of debris flow solid fraction on rigid barrier impact. *Can Geotech J*. doi:10.1139/cgj-2016-0502
- Takahashi T (2014) *Debris flow: mechanics, prediction and countermeasures*. CRC Press, Boca Raton
- Take WA (2015) Thirty-sixth Canadian geotechnical colloquium: advances in visualization of geotechnical processes through digital image correlation. *Can Geotech J* 52(9):1199–1220
- Wendeler C, McArdell BW, Rickenmann D, Volkwein A, Roth A, Denk M (2006) Field testing and numerical modeling of flexible debris flow barriers. In *Proceedings of international conference on physical modelling in geotechnics*, Hong Kong
- Wendeler C, Volkwein A, Denk M, Roth A, Wartmann S (2007) Field measurements used for numerical modelling of flexible debris flow barriers. In CL Chen, JJ major (eds). *Proceedings of Fourth International Conference on Debris Flow Hazards Mitigation: Mechanics, Prediction, and Assessment*, Chengdu, China, 10–13 September 2007. Pp. 681–687
- Wendeler C (2016) Debris flow protection systems for mountain torrents—basic principles for planning and calculation of flexible barriers. *WSL Bericht* 44. ISSN 2296-3456
- Wendeler C, Volkwein A (2015) Laboratory tests for the optimization of mesh size for flexible debris-flow barriers. *Nat Hazards Earth Syst Sci* 15(12):2597–2604
- White DJ, Take WA, Bolton MD (2003) Soil deformation measurement using particle image velocimetry (PIV) and photogrammetry. *Geotechnique* 53(7):619–631
- WSL (2009) Full-scale testing and dimensioning of flexible debris flow barriers. Technical report 1–22. WSL, Birmensdorf
- Zhou GGD, Ng CWW (2010) Dimensional analysis of natural debris flows. *Can Geotech J* 47(7):719–729

**D. Song · G. G. D. Zhou**

Key Laboratory of Mountain Hazards and Earth Surface Process/Institute of Mountain Hazards and Environment, Chinese Academy of Sciences (CAS), Chengdu, China

**D. Song**

e-mail: drsong@imde.ac.cn

**G. G. D. Zhou**

e-mail: gordon@imde.ac.cn

**D. Song · G. G. D. Zhou**

University of Chinese Academy of Sciences, Beijing, China

**D. Song · C. E. Choi (✉) · C. W. W. Ng**

Department of Civil and Environmental Engineering, Hong Kong University of Science and Technology, Clear Water Bay, Kowloon, Hong Kong  
e-mail: ceclarence@ust.hk

**C. W. W. Ng**

e-mail: cecwng@ust.hk

**C. E. Choi**

HKUST Jockey Club Institute for Advanced Study, Hong Kong University of Science and Technology, Clear Water Bay, Kowloon, Hong Kong